

## Full length article

## Precipitation hardening of an Mg–5Zn–2Gd–0.4Zr (wt. %) alloy

J.H. Li<sup>a, \*</sup>, J. Barrirero<sup>b</sup>, G. Sha<sup>c</sup>, H. Aboufadel<sup>b</sup>, F. Mücklich<sup>b</sup>, P. Schumacher<sup>a, d</sup><sup>a</sup> Institute of Casting Research, Montanuniversität Leoben, A-8700, Leoben, Austria<sup>b</sup> Department of Materials Science, Saarland University, Campus D3.3, D-66123 Saarbrücken, Germany<sup>c</sup> School of Materials Science and Engineering, Nanjing University of Science and Technology, Nanjing, 210014, China<sup>d</sup> Austrian Foundry Research Institute, A-8700, Leoben, Austria

## ARTICLE INFO

## Article history:

Received 5 November 2015

Accepted 23 January 2016

Available online xxx

## Keywords:

Magnesium alloy

Precipitation hardening

TEM

Atom probe tomography

## ABSTRACT

Mg–5Zn–2Gd–0.4Zr alloy (wt. %) shows a significant age hardening response with a hardness increment from 62 HV to 72 HV by ageing at 200 °C for up to 80 h. Transmission electron microscopy and atom probe tomography characterizations reveal that precipitates with different morphologies and habit planes form in the alloy, including triangular-shaped ZnZr phase, rectangular-shaped Zn<sub>2</sub>Zr phase, [0001]<sub>Mg</sub> rods ( $\beta'_1$ ) MgZn<sub>2</sub> Laves phase, (0001)<sub>Mg</sub> plate ( $\beta'_2$ ) MgZn<sub>2</sub> Laves phase, and coherent GP zones. Furthermore, a significant partitioning of Gd into Zn-rich precipitates ( $\beta'_1$  and  $\beta'_2$ ) was, for the first time, observed, which is considered to be responsible for improving the thermal stability of Zn-rich precipitates and enhancing the precipitation hardening of the alloy. A core–shell structure with the shell of Gd (~2 at%) and the core of Zn<sub>2</sub>Zr phase was also observed, which is proposed to hinder the coarsening of Zn<sub>2</sub>Zr phase. No further change in average size of the Zn<sub>2</sub>Zr particles was observed after ageing over 15 h. Better understanding the partitioning of Gd into the Zn-rich precipitates and the formation of the core–shell structures are essential to control the precipitation microstructure and develop high performance Mg alloys.

© 2016 Acta Materialia Inc. Published by Elsevier Ltd. All rights reserved.

## 1. Introduction

Magnesium alloys have a great potential for automotive and aerospace applications due to their high specific strength [1]. Mg–Zn binary alloys can exhibit a remarkable age hardening response at room temperature by controlling the decomposition of the supersaturated solid solution of Zn in Mg [2,3]. However, the precipitates formed in binary Mg–Zn alloys during artificial ageing are generally coarse in size and have inhomogeneous distribution in the Mg matrix. Furthermore, the thermal stability of the precipitates in the binary Mg–Zn alloys decreases sharply with increasing temperatures [3]. The high temperature mechanical properties of these Mg–Zn binary alloys are, therefore, inadequate for technological applications at temperatures above 250 °C [4,5].

Multiple alloying element addition has been widely used in Mg alloys. Zr addition can refine the grain size and thereby improve strength [6,7]. However, a loss of age hardening response has been observed, which is attributed to the fact that the formation of Zn–Zr phases partly consumes Zn and thereby greatly reduces the

fraction of Zn-rich precipitates [8], although Zn–Zr phases may also play a role for hardening the alloy [9]. Other alloying elements, i.e. Cr [10], Cu [11–14], Ba [15], Ag [16], Ca [17], Ag and Ca [18,19], V [20], Sn [21], RE (Y [22], Nd [23], Gd [24–28], MM (misch metal) [29,30], Er [31]), were added to Mg–Zn binary alloys containing Zr, with the aim to modify the precipitation microstructure and thereby improve the precipitation hardening. Among these elements, Gd has been used more often since the solid solubility of Gd in Mg at 548 °C is about 4.53 at % (23.49 wt %), and decreases to 0.61 at % (3.82 wt %) at 200 °C [2], resulting in an excellent age hardening response. Mg–Zn–Gd based alloys are, therefore, thought to be a promising system for further developments. Mg–5Zn–2Gd–0.4Zr alloy (wt. %) was found to exhibit optimal mechanical properties [26]. It has been reported that the as-cast microstructure was composed of  $\alpha$ (Mg) matrix, interdendritic  $\alpha$ (Mg) + W(Mg<sub>3</sub>Zn<sub>3</sub>Gd<sub>2</sub>) eutectic, icosahedral quasicrystalline I(Mg<sub>3</sub>Zn<sub>6</sub>Gd), Mg<sub>3</sub>Gd phase and  $\alpha$ (Zr) particles [26]. A solution treatment (at 500 °C for 18 h) can dissolve interdendritic  $\alpha$ (Mg) + W(Mg<sub>3</sub>Zn<sub>3</sub>Gd<sub>2</sub>). After the ageing treatment (at 200 °C for 15 h), metastable phases, rod-like  $\beta'_1$  and plate-like  $\beta'_2$ , were observed within the  $\alpha$ (Mg) matrix. The precipitation microstructure evolution in Mg–Zn–Gd based alloy as a function of ageing

\* Corresponding author.

E-mail address: [jie-hua.li@hotmail.com](mailto:jie-hua.li@hotmail.com) (J.H. Li).

time has attracted significant attention [24–28]. However, solute clustering, metastable precipitate and stable precipitate formation in Mg–Zn–Gd based alloys have been not fully understood yet. Especially, there is still a lack of information on the solute partitioning of Gd into these precipitates. Thus, the role of Gd during ageing still remains to be explored.

In this paper, correlative transmission electron microscopy (TEM) and atom probe tomography (APT) was used to investigate the precipitation microstructure evolution in Mg–5Zn–2Gd–0.4Zr (wt. %) alloy, with the aim to elucidate its precipitation hardening. TEM was employed to characterize the structure properties of the different precipitates in the alloy during ageing, while APT was used to reveal local compositions and cluster distribution at the atomistic level, with a special focus on the partitioning behavior of Gd in the alloy during ageing. The detailed structural and chemical composition information helps to elucidate the strengthening effects of these precipitates and thereby provide useful hints to develop high performance Mg alloys.

## 2. Experimental methods

The Mg–5Zn–2Gd–0.4Zr alloy (wt. %, named as ZG52, used throughout the paper in case not specified otherwise) was prepared from pure Mg (99.9%), Zn (99.9%), Mg–28Gd and Mg–33Zr master alloys in an electric resistance furnace under the protection of an anti-oxidizing flux, and then cast into a sand mould. Solution treatment was performed in a salt bath at 500 °C for 18 h, followed by quenching into cold water and then subsequently aged in oil bath at 200 °C for up to 100 h.

Optical microscopy (OM) characterization was performed using Zeiss Axioskop 2 MAT light microscope. Vickers hardness testing was performed using a LECO Hardness Tester (LV700AT) with 50 N load and 15 s dwell time. Each data point reported in this paper represents an average of at least 10 measurements. The samples for TEM investigation under three ageing conditions (0.5 h, 15 h and 80 h) were mechanically grounded, polished and dimpled to about 30 µm in thickness, and then ion-beam milled using a Gatan Precision Ion Polishing System (PIPS, Gatan model 691). A preparation temperature (about –10 °C) was kept constant by using a cold stage during ion beam polishing. TEM, high resolution TEM (HRTEM) micrographs and energy dispersive X-ray spectra (EDX) investigations were performed using a Cs-corrected JEOL-2100F microscope operated at 200 kV.

The samples for APT investigation under the three ageing conditions (0.5 h, 15 h and 80 h) were prepared by the standard lift-out technique [32] in a dual-beam focused ion beam/scanning electron microscopy workstation (FIB/SEM) (Helios NanoLab 600™, FEI Company, USA). It should be noted here that the samples for TEM and APT were taken from the same bulk samples in order to obtain a consistent and comparable observation. The lift-outs were all extracted from the center of Mg grains, which are known to be Zr-rich regions [12]. After thinning the specimens, a low energy milling at 2 kV was performed to minimize Ga induced damage. APT was carried out in a LEAP™ 3000X HR (CAMECA) in voltage mode with a pulse fraction of 20% and a repetition rate of 200 kHz. Specimen temperature of about 40 K, pressure lower than  $1 \times 10^{-10}$  Torr ( $1.33 \times 10^{-8}$  Pa) and evaporation rate of 5 atoms per 1000 pulses were maintained for all measurements. Datasets were reconstructed and analyzed with IVAS™3.6.8 software (CAMECA).

The composition of precipitates was extracted by the envelope method from the 3D reconstructions for cluster identification with Zn and Gd as clustering solutes [33]. A maximal separation distance of 0.7 nm was derived from a Count Distribution Analysis (CDA) and confirmed by a Nearest-Neighbor Analysis (NNA) in IVAS software. A minimal cluster size of  $N_{\min} = 10$  was used to filter out small

clusters. Matrix atoms with a surrounding distance of up to 0.7 nm were included in the cluster and subsequently eroded by the same distance.

## 3. Results

### 3.1. Microstructures of as-cast, solution treated and aged ZG52 alloy

Fig 1 shows the microstructures of as-cast, solution treated and aged ZG52 alloy, respectively. The microstructure of the as-cast sample was composed of equiaxed  $\alpha$ -Mg grains surrounded by eutectic compound ( $\alpha(\text{Mg}) + \text{W}(\text{Mg}_3\text{Zn}_3\text{Gd}_2)$ ) at triple junctions and grain boundaries, as shown in Fig. 1a. The mean grain size of as-cast ZG52 alloy was measured to be approximately  $35 \pm 5$  µm using a linear intercept method, which is close to that of a ZK60 (Mg–6Zn–0.4Zr) alloy with 1.3 wt. % Gd addition, but much less than that of ZK60 alloy (71 µm) [22,24]. Clearly, the addition of Gd (2 wt.%) significantly refines the grain size of Mg–Zn based alloys, which can be attributed to the increasing growth restriction caused by Gd and/or the partitioning of Gd into Zr-containing particles as well as the formation of core–shell structures, as described in section 3.4. After a solution treatment at 500 °C for 18 h, most of the secondary phase was dissolved into the  $\alpha$ -Mg matrix, as shown in Fig. 1b. Furthermore, flower-like regions, known to be Zr-rich or Zn-rich [12,26], were observed after the solution treatment at 500 °C for 18 h, as shown in Fig. 1b. After a subsequent ageing treatment at 200 °C for 15 h, more secondary phase formed along the grain boundaries, as shown in Fig. 1c.

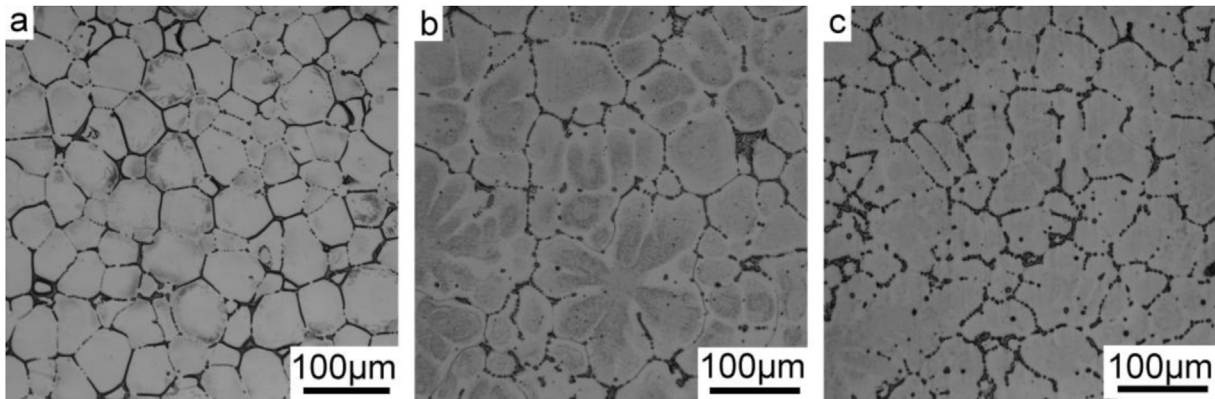
### 3.2. Age hardening response of the ZG52 alloy

Fig 2 shows the age hardening response of the ZG52 alloy at 200 °C up to 100 h. No significant change of the hardness was observed at the beginning of the ageing treatment within 50 h. Such phenomenon was also observed in an Mg–4.5Zn–2Gd (wt. %) alloy [24]. The peak hardness (72 HV) was observed at about 80 h. The peak hardness value (72 HV) of ZG52 alloy is equivalent to that of the Mg–8Zn–1.5RE (MM, a mixture of approximately 50Ce, 25La, 20Nd, and 3Pr) and Mg–4Zn–1.5RE (MM), but considerably greater than that of binary Mg–9Zn alloy according to hardness values reported in literature [29]. Moreover, the peak hardness occurred at about 80 h ageing for ZG52 alloy, which is much later than 10 h for Mg–9Zn alloy and 20 h for Mg–8Zn–1.5RE and Mg–4Zn–1.5RE, respectively. This clearly indicates that the addition of Gd into Mg–Zn alloy postpones the age-hardening response of the alloy. On the basis of the age hardening response of the ZG52 alloy, three samples under three ageing conditions (0.5 h, 15 h and 80 h) were further investigated using high resolution techniques (TEM and APT).

### 3.3. TEM characterization of precipitates in the ZG52 alloy

#### 3.3.1. Zr-rich precipitates

Fig 3 shows bright field TEM image, HRTEM image, corresponding fast Fourier Transform (FFT) and EDX analysis of one triangular-shaped Zr-rich phase in ZG52 alloy aged at 200 °C for 0.5 h. The Zr-rich phase has been reported to be  $\text{Zn}_2\text{Zr}_3$  phase [14,26] or  $\text{Zn}_3(\text{Zr}_{1-\gamma}\text{Mg}_\gamma)_2$  phase [12], although both phases have a similar tetragonal  $\text{U}_3\text{Si}_2$  type crystal structure with a lattice of  $a = 0.763$  nm,  $c = 0.696$  nm. However, EDX analysis (Fig 3e) indicates that Zr-rich phase in the present investigation contains about 45 at% Zn, 46 at% Zr and 9 at% Mg. The ratios of Zn:Zr is close to 1:1. The Zr-rich phase is, therefore, more likely to be ZnZr phase (Pm–3m(221),  $a = 0.3336$  nm) [34]. It should be noted that the Mg



**Fig. 1.** Optical microscopy microstructure of ZG52 alloy. (a) in as-casting condition; (b) after a solution treatment at 500 °C for 18 h; (c) after a solution treatment at 500 °C for 18 h and subsequent ageing treatment at 200 °C for 15 h. Zr-rich region (flower-like) was observed in (b).

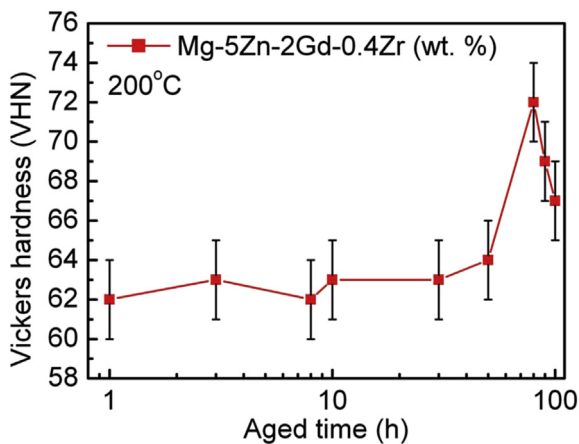


**Fig. 2.** Age hardening response of ZG52 alloy aged at 200 °C up to 100 h.

concentration from the scan may be affected by the surrounding matrix. The size of the ZnZr particles is defined as  $L_P$  (Fig 3a) and was measured to be about  $96 \pm 23$  nm from at least 53 measurements (Table 1). The ZnZr phase forms during solidification and survives during solution treatment (500 °C for 18 h), as shown in Fig. 1b (flower-like region).

Apart from the triangular-shaped ZnZr phase, one rectangular-shaped Zr-rich phase was also observed in ZG52 alloy aged at 200 °C for 0.5 h, as shown in Fig 4. EDX analysis (Fig 4e) indicates that Zr-rich phase contains about 65 at% Zn and 35 at% Zr. The ratios of Zn:Zr is close to 2:1, which can be indexed as  $Zn_2Zr$  phase (Fd-3m O1 (227),  $a = 0.7397$  nm) [35]. As reported in Refs. [8,9], the  $Zn_2Zr$  phase forms during solution treatment and/or ageing treatment. It should be noted that no significant Mg concentration was observed within the  $Zn_2Zr$  phase. The EDX analysis can be, therefore, used to unambiguously distinguish the  $Zn_2Zr$  phase and  $MgZn_2$  Laves phase despite their similar morphology. The geometry and size of the rectangular-shaped  $Zn_2Zr$  phase is defined as  $L_R$  (Length) and  $W_R$  (Width) (Fig 4a), respectively.

With increasing ageing time from 0.5 h to 15 h, the average length of  $Zn_2Zr$  particles increases to  $313 \pm 16$  nm ( $L_R$ ), but the width (or thickness) decreases to  $16 \pm 4$  nm ( $W_R$ , taken from at least 149 measurements) (Table 2), indicating that  $Zn_2Zr$  phase favorably grows along its length in  $[0001]_\alpha$  direction. This ensures a minimal interface misfit between the  $Zn_2Zr$  phase and  $\alpha$ -Mg matrix. It should be noted here that it is not possible to obtain the information of the volume fraction of  $Zn_2Zr$  particles on the basis of their

length and width in two dimensional. However, a statistical analysis of such two dimensional information can provide a reasonable prediction to the growth of  $Zn_2Zr$  phase. Fig 5 shows bright field TEM image, HRTEM image, corresponding FFT and EDX analysis of one plate-shaped  $Zn_2Zr$  phase in ZG52 alloy aged at 200 °C for 15 h. A coherent orientation relationship (OR, i.e.  $\langle 1120 \rangle_{Mg} // \langle 112 \rangle_{Zn_2Zr}$ ,  $\{0002\}_{Mg} // \{(111)_{Zn_2Zr}\}$ ) was observed between  $Zn_2Zr$  phase and Mg matrix (Fig 5b,c,d). Interestingly, further increasing the ageing time to 80 h results in a decreased length of  $Zn_2Zr$  phase ( $274 \pm 122$  nm from at least 160 measurements), but an increased width (or thickness) ( $W_R$ ) ( $27 \pm 11$  nm) (Table 2), indicating that the coarsening of  $Zn_2Zr$  phase was hindered. This can be attributed to the fact that these  $Zn_2Zr$  particles precipitated during solution treatment at 500 °C, which is believed to serve as a heterogeneous nucleation site for the precipitation of  $\beta_1'$ - $MgZn_2$  Laves phase during the subsequent ageing treatment at 200 °C [12], gradually decomposed with the growth of the successor  $\beta_1'$ - $MgZn_2$  Laves phase, and thereby the released Zr atoms diffused into the matrix or involved into the formation of new Zr-containing compounds. Indeed, most  $Zn_2Zr$  phase is still relatively small in size with increasing ageing time, which can be expected to strengthen the alloy. Fig. 6 shows bright field TEM image, HRTEM image, corresponding FFT and EDX analysis of one plate-shaped  $Zn_2Zr$  phase in ZG52 alloy aged at 200 °C for 80 h. A coherent OR (i.e.  $\langle 1120 \rangle_{Mg} // \langle 112 \rangle_{Zn_2Zr}$ ,  $\{0002\}_{Mg} // \{(111)_{Zn_2Zr}\}$ ) was still kept between  $Zn_2Zr$  phase and Mg matrix (Fig 6b,c,d). It should be noted here that the distribution of  $Zn_2Zr$  phase is not homogeneous. In the Zr-rich regions (i.e. in the center of Mg grain), more  $Zn_2Zr$  phase was observed, as shown in Figs. 3–6. However, in the Zr-lean regions, less or no (if any)  $Zn_2Zr$  phase was observed. Instead, more Zn-rich precipitates were detected, as shown in section 3.3.2.

### 3.3.2. Zr-rich precipitates

Apart from the Zr-rich phases, no significant Zn-rich precipitates (i.e.  $[0001]_{Mg}$  rod ( $\beta_1$ )  $MgZn_2$  Laves phase,  $(0001)_{Mg}$  plate or block ( $\beta_2$ )  $MgZn_2$  Laves phase) were found in ZG52 alloy aged at 200 °C for 0.5 h. However, such Zn-rich precipitates were observed after ageing at 200 °C for 15 h and 80 h, respectively. Fig. 7 shows  $[2\bar{1}\bar{1}0]$  bright field TEM image and corresponding selected area diffraction pattern (SADP) of Zn-rich precipitates within the  $\alpha$ -Mg matrix in the ZG52 alloy aged at 200 °C for 15 h. The Zn-rich precipitates are present with two different morphologies, i.e.  $[0001]_\alpha$  rod and  $(0001)_\alpha$  plate, as shown in Fig 7a. The  $[0001]_\alpha$  rod has been commonly regarded as  $\beta_1'$ , while the  $(0001)_\alpha$  plate was commonly taken as  $\beta_2'$  in previous reports [29,30]. Both  $\beta_1'$  and  $\beta_2'$  are indexed to have a hexagonal structure ( $a = 0.523$  nm,  $c = 0.858$  nm) [29,30],

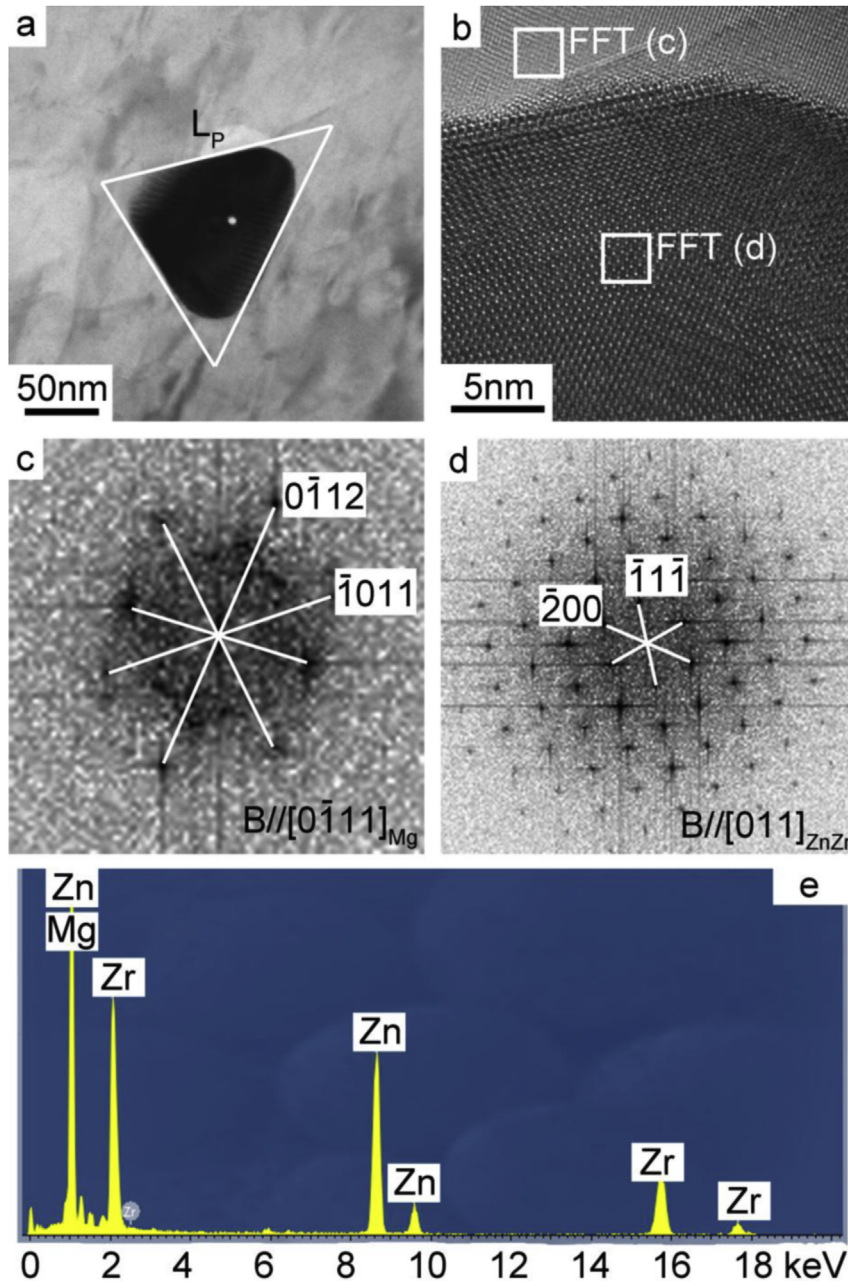


**Fig. 3.** Bright field TEM image (a), HRTEM image (b), corresponding FFT (c) (d) and EDX analysis (e) of one triangular-shaped ZnZr phase in ZG52 alloy aged at 200 °C for 0.5 h.

**Table 1**  
Spacing measurement ( $L_p$ ) of triangular-shaped ZnZr phase.

Time (h)	Spacing (nm)	$\sigma$ (nm)	N
0.5	96	23	53
15	34	16	4
80	94	25	18

$\sigma$  Standard deviation.

N Number of measurements made.

which is identical to that of  $MgZn_2$  Laves phase [29,30], although  $\beta'_1$  has been also reported to be  $Mg_2Zn_3$  phase [2,12] and  $Mg_4Zn_7$  monoclinic phase with a lattice parameter  $a = 2.596$  nm,  $b = 0.524$  nm,  $c = 1.428$  nm,  $\beta = 102.5^\circ$  [36].

With increasing ageing time from 15 h to 80 h, both  $\beta'_1$  and  $\beta'_2$

still co-exist, as shown in Fig. 8. More interestingly, the size of  $\beta'_1$  and  $\beta'_2$  phase does not appear to increase significantly, indicating that a prolonged ageing at 200 °C does not lead to a significant coarsening of  $\beta'_1$  and  $\beta'_2$  phase. The number density of the  $[0001]_\alpha$  rod with a larger aspect ratio on the cross section (Fig. 8), are still dominant after ageing at 200 °C for 80 h. This is in contrast to the previous reports in Mg–Zn alloy [29,30] and other Mg–Zn–RE alloy [30], where  $[0001]_\alpha$  rod ( $\beta'_1$ ) were reported to transform into  $(0001)_\alpha$  plate ( $\beta'_2$ ), and the  $\beta'_2$  precipitates became dominant in the microstructure with increasing ageing time. It is generally understood that the formation of a fine dispersion of rod-shaped  $\beta'_1$  precipitates plays an important role for the precipitation hardening, while an extensive precipitation of plate-shaped  $\beta'_2$  precipitates coincides with an onset of overageing [30]. In the present investigation, the dominant distribution of the rod-shaped  $\beta'_1$

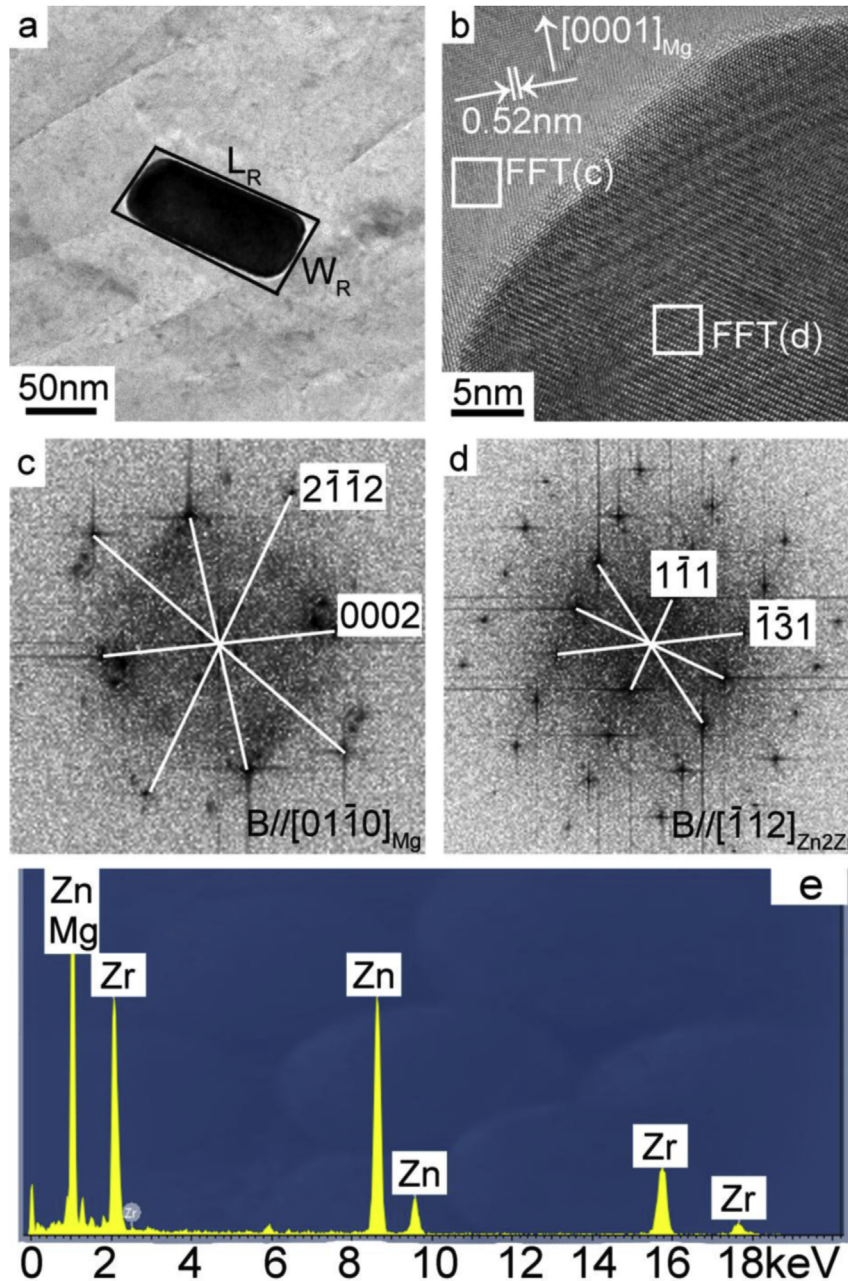


**Fig. 4.** Bright field TEM image (a), HRTEM image (b), corresponding FFT (c) (d) and EDX analysis (e) of one rectangular-shaped Zn<sub>2</sub>Zr phase in ZG52 alloy aged at 200 °C for 0.5 h.

**Table 2**  
Spacing measurement of rectangular-shaped Zn<sub>2</sub>Zr phase.

	Time (h)	Spacing (nm)	σ (nm)	N
L <sub>R</sub>	0.5	182	104	72
	15	313	16	149
	80	274	122	160
W <sub>R</sub>	0.5	42	17	72
	15	16	4	149
	80	27	11	160

σ Standard deviation.

N Number of measurements made.

precipitates after ageing at 200 °C for 80 h strongly indicates the addition of Gd delays precipitation and enhances the peak hardness in ZG52 alloy. This may partly account for the reason why the peak

hardness (72 HV) of ZG52 alloy was achieved at 80 h (see Fig. 2).

### 3.3.3. GP zones

Apart from the Zr-rich phases (ZnZr phase and Zn<sub>2</sub>Zr phase) and Zn-rich phase ( $\beta_1$  phase,  $\beta_2$  phase), coherent GP zones habiting on prism planes (i.e. {1120} or {0110}) were also observed in ZG52 alloy aged at 200 °C for 15 h and 80 h, respectively, as shown in Fig. 9. This is fully consistent with the previous report in Mg–Zn alloy [4], where the GP zones have been defined as GP1 zones. When aged at 200 °C for 15 h, the coherent GP zones are only  $22 \pm 5$  nm in length and  $1.4 \pm 0.1$  nm in thickness (Table 3), as shown in Fig. 9a. Increasing the ageing time from 15 h to 80 h, the size of the coherent GP zones increases to  $26 \pm 5$  nm in length,  $2 \pm 0.3$  nm in thickness (Table 3), as shown in Fig. 9b,c. However, the number density of the coherent GP zones appears to decrease. It

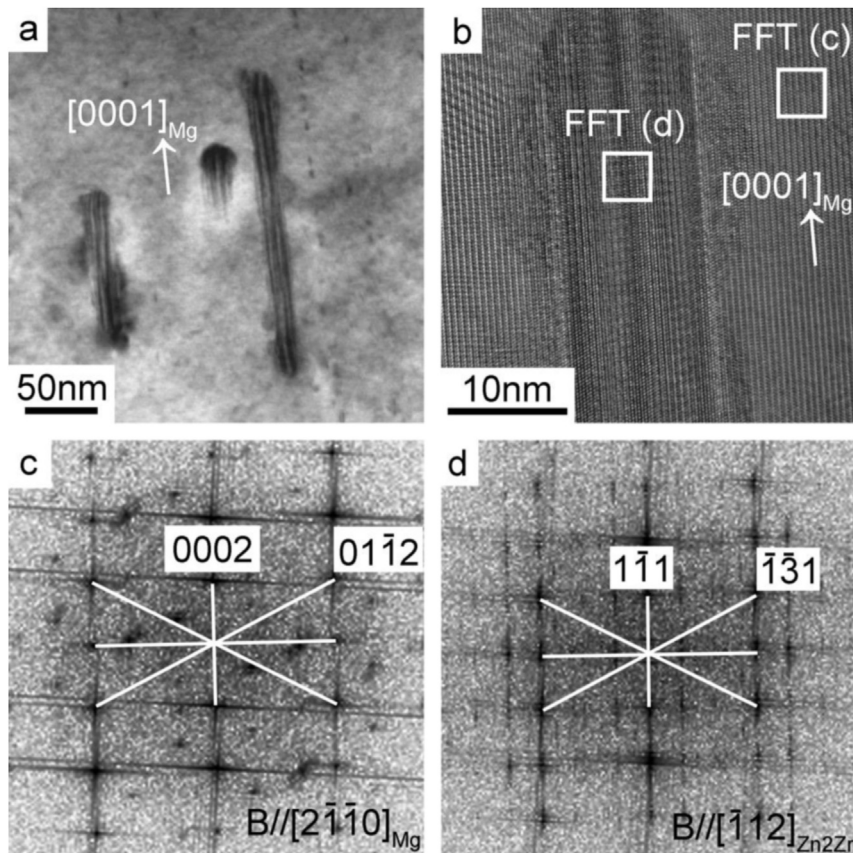


**Fig. 5.** Bright field TEM image (a), HRTEM image (b) and corresponding FFT (c) (d) of one plate-shaped  $\text{Zn}_2\text{Zr}$  phase in ZG52 alloy aged at 200 °C for 15 h.

should be noted here that both the coherent GP zones and Zn-rich precipitates are habiting on prism planes (i.e.  $\{1120\}$  or  $\{0110\}$ ), respectively. It is very likely that the coherent GP zones are metastable and transform into Zn-rich precipitates, which can be further supported by our APT investigation.

#### 3.4. APT characterization of the precipitates in the ZG52 alloy

##### 3.4.1. Zn-rich precipitates

**Fig. 10** shows the microstructural evolution of Zn-rich precipitates in the ZG52 alloy aged at 200 °C for 0.5 h, 15 h, and 80 h, respectively. At the initial condition (0.5 h, **Fig. 10a**), fine compositional oscillations were observed, which can be attributed to solute clustering of Mg, Zn and Gd during the early stage of ageing. This reconstruction represents the regions outside the ZnZr and  $\text{Zn}_2\text{Zr}$  precipitates, as shown in **Fig. 3a** and **4a**. Furthermore, no Zn-rich precipitates were observed. After ageing at 200 °C for 15 h, spherical clusters containing between 100 and 1000 atoms with a diameter of 1–2 nm were observed, as shown in **Fig. 10b**. It should be noted here that due to the small volume probed by APT [37] only spherical clusters were detected at this stage from several measurements. The number density of the spherical clusters is estimated to be  $2.66 \times 10^{23} \text{ m}^{-3}$ . The average composition of 165 spherical clusters detected from 4 APT specimens is about  $61.47 \pm 0.06 \text{ at\% Mg}$ ,  $30.56 \pm 0.05 \text{ at\% Zn}$ ,  $7.14 \pm 0.02 \text{ at\% Gd}$  and  $0.16 \pm 0.01 \text{ at\% Zr}$ , as listed in **Table 4**. The ratio of Mg and Zn is about 2:1, indicating that such type of spherical cluster can be attributed to the  $\text{Mg}_2\text{Zn}$  phase. The  $\text{Mg}_2\text{Zn}$  phase appears to be related to metastable GP zones detected by TEM (**Fig. 9a**). The metastable  $\text{Mg}_2\text{Zn}$  phase may transform into stable Zn-rich precipitates (i.e.

$\text{MgZn}$ , not detected here) if Zn further partitions into  $\text{Mg}_2\text{Zn}$  phase. Indeed, after ageing at 200 °C for 80 h, not only spherical clusters but also larger disc-shaped precipitates were observed, as shown in **Fig. 10c**. In total, 4 APT specimens were analyzed from 80 h ageing sample which included: (i) 40 spherical clusters with a diameter of 1–2 nm, (ii) 18 disc-shaped precipitates with a thickness of ~2 nm and a diameter ranging from 5 nm to 25 nm. The number density of spherical clusters is estimated to be  $0.47 \times 10^{23} \text{ m}^{-3}$ , which is much less than that in the alloy aged at 200 °C for 15 h, confirming that spherical clusters are metastable and indicating that a fraction of the spherical clusters in 15 h has vanished, while others grow by Ostwald ripening and transform into stable precipitates. The average composition for the spherical cluster is measured to be about  $59.37 \pm 0.12 \text{ at\% Mg}$ ,  $29.38 \pm 0.09 \text{ at\% Zn}$ ,  $9.26 \pm 0.04 \text{ at\% Gd}$  and  $1.05 \pm 0.04 \text{ at\% Zr}$ , as listed in **Table 4**. Compared with 15 h, more Gd and Zr were measured within the spherical clusters. The number density of disc-shaped precipitates is estimated to be  $0.21 \times 10^{23} \text{ m}^{-3}$ . The average composition for the disc-shaped precipitates is measured to be about  $67.94 \pm 0.03 \text{ at\% Mg}$ ,  $21.75 \pm 0.02 \text{ at\% Zn}$ ,  $9.57 \pm 0.01 \text{ at\% Gd}$  and  $0.12 \pm 0.01 \text{ at\% Zr}$ , as listed in **Table 4**. However, no significant composition differences between spherical cluster and disc-shaped precipitates were observed. The ratio of Mg and Zn (together with Gd) is about 2:1, indicating that such disc-shaped precipitates can be also metastable and are about to transform into stable Zn-rich precipitates. Furthermore, disc-shaped precipitates show a lower Zn content of about 23 at% and a higher Gd content of 10 at% when compared with the spherical cluster. This indicates that Gd partitions into disc-shaped precipitates, as shown in an enlarged image from **Fig. 10c**. All observations indicate that disc-shaped precipitates may

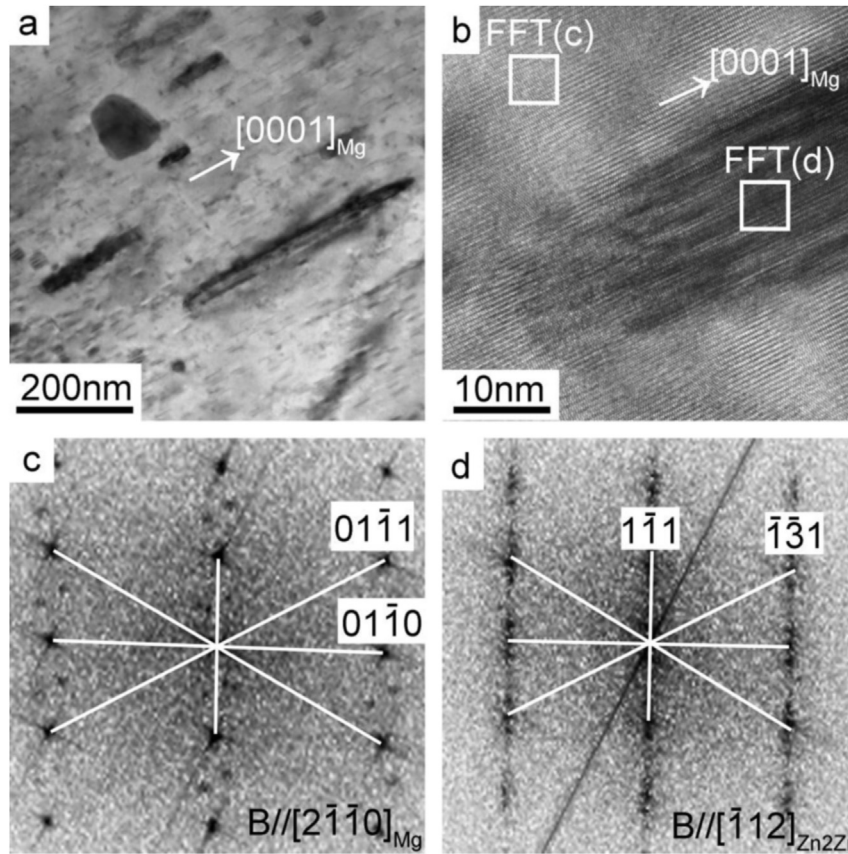


Fig. 6. Bright field TEM image (a), HRTEM image (b) and corresponding FFT (c) (d) of one plate-shaped  $Zn_2Zr$  phase in ZG52 alloy aged at 200 °C for 80 h.

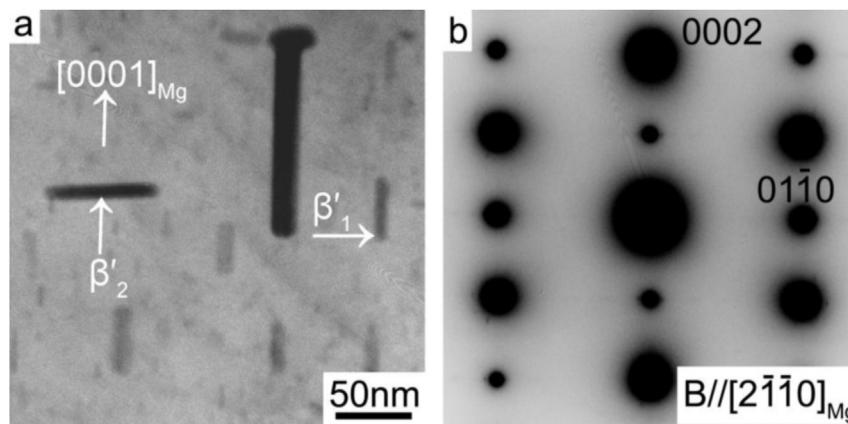


Fig. 7.  $[2\bar{1}\bar{1}0]_{\alpha}$  bright field TEM image (a), corresponding SADP (b) of  $[0001]_{\alpha}$  rod ( $\beta'_1$ ) and  $(0001)_{\alpha}$  plate ( $\beta'_2$ ) in ZG52 alloy aged at 200 °C for 15 h.

originate from spherical clusters.

### 3.4.2. Zr-rich precipitates

Fig. 11 shows one Zr-rich precipitate with a core–shell structure from the ZG52 alloy aged at 200 °C for 80 h. Only a fraction of this precipitate was detected in the APT reconstruction. It is, therefore, not possible to report the size or morphology of the complete precipitate, although it is clear that it corresponds to the corner of a large Zr-rich phase, as shown in TEM (section 3.3.1). The average composition of the core is ~46 at% Zn, ~29 at% Zr, ~3 at% Mg, ~0.5 at% Gd and ~20 at% H. This composition agrees with the  $Zn_3(Zr_{1-x}Mg_x)_2$  reported by Ref. [12]. Interestingly, the core is surrounded by a Gd-

rich shell of about 2 at% Gd.

In the vicinity of the Zr-rich phase, a Zn-Gd-rich compound was measured with a composition of ~53 at% Mg, 37 at% Zn and 8.8 at% Gd. This indicates that the Zn-Gd-rich compound can be related to the Zn-rich precipitates, as reported in the previous section 3.3.2. This also indicates that the Zr-rich phase may be related to the heterogeneous nucleation of Zn-rich precipitates. These findings are in agreement with the Zr- and Zn-rich segments reported by Refs. [12,13]. It should be noted that the hydrogen value reported here (~20 at%) can have slight errors due to the residual hydrogen in the chamber which interacts with the field evaporation process [38]. The beneficial effect of H on the formation of Zr-rich

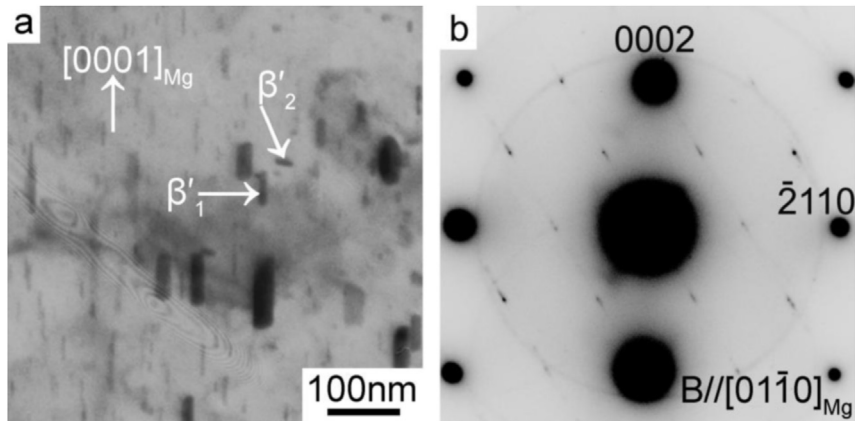


**Fig. 8.**  $[01\bar{1}0]_{\alpha}$  bright field TEM image (a), corresponding SADP (b) of  $[0001]_{\alpha}$  rod ( $\beta'_1$ ) and  $(0001)_{\alpha}$  plate ( $\beta'_2$ ) in ZG52 alloy aged at 200 °C for 80 h.

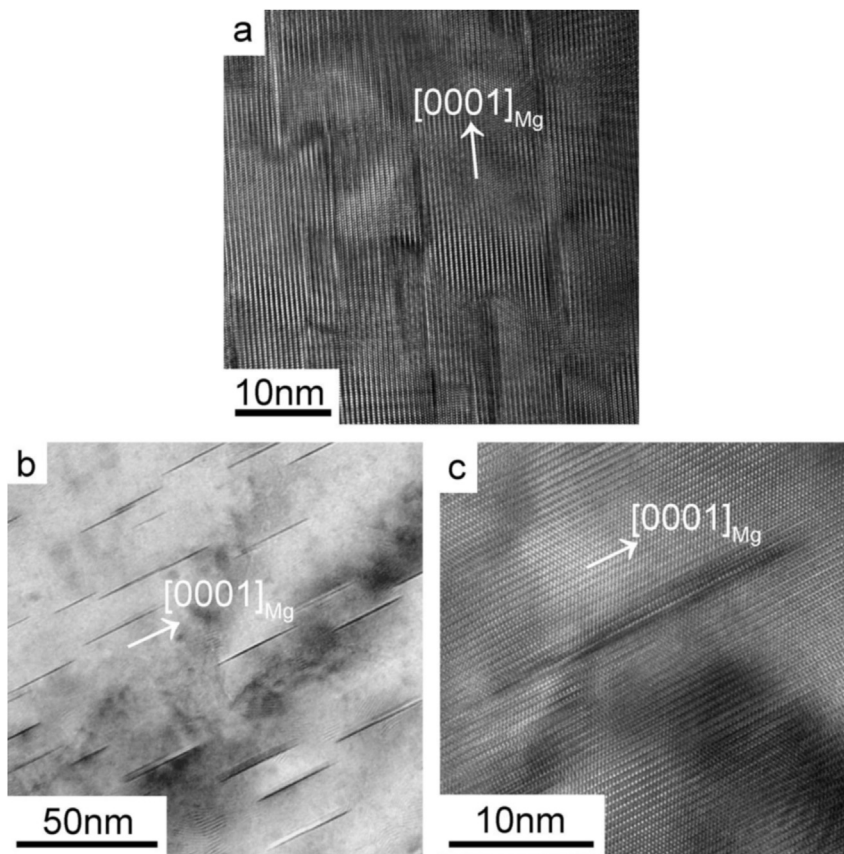


**Fig. 9.** HRTEM images of the GP zone and/or prismatic precipitates in ZG52 alloy aged at 200 °C for 15 h (a) and 80 h (b), (c). (c) is enlarged from (b).

**Table 3**  
Spacing measurement of coherent GP zones.

Time (h)	Length (nm)	Thickness (nm)	N
15	22 ± 5	1.4 ± 0.1	7
80	26 ± 5	2 ± 0.3	22

$\sigma$  Standard deviation.

N Number of measurements made.

precipitates has been reported in Ref. [12] via APT technique. A detailed discussion about the roles of H is beyond the scope of the present investigation.

## 4. Discussion

### 4.1. Precipitation of Zr-rich precipitates

In the Zr-rich regions (i.e. in the center of Mg grain), Zr-rich phases ( $\text{ZnZr}$  phase and  $\text{Zn}_2\text{Zr}$  phase) were observed, as shown in Figs. 3–6. The formation of Zr-rich phases has been attributed to the adsorption of Zn in Zr particle [39]. Furthermore, when solution treatment was performed at elevated temperatures for a long time (i.e. 500 °C for 18 h in the present investigation), Zr also diffuses from the Zr-rich zone (in the center of Mg grain) to the neighboring regions. Both factors affect the formation of Zr-rich phases. The

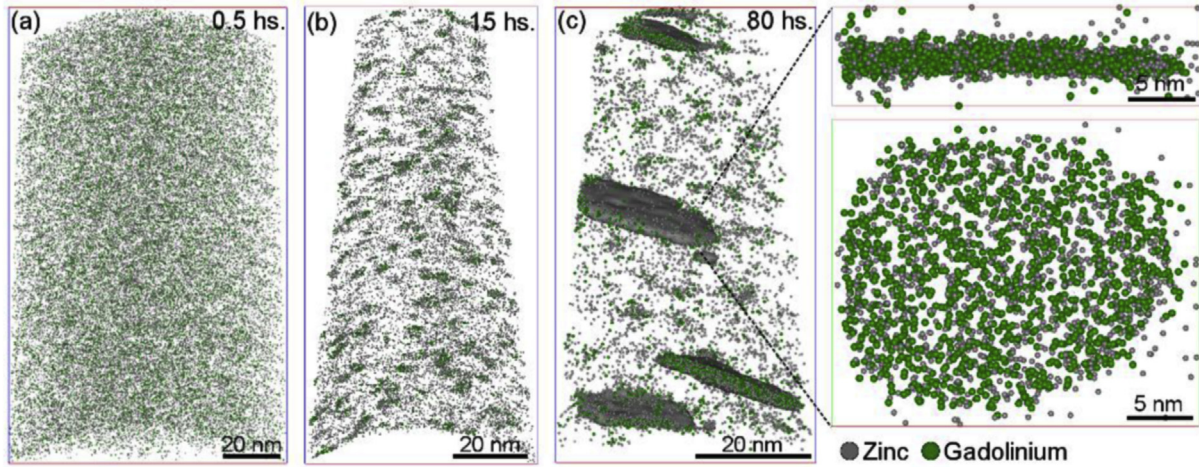


**Fig. 10.** Atomic maps showing the microstructural evolution of the ZG52 alloy aged at 200 °C for (a) 0.5 h, (b) 15 h, and (c) 80 h, respectively. An image is enlarged from (c) to show the partitioning of Gd into disc-shaped precipitates.

**Table 4**

Average composition of the spherical cluster and disc-shaped precipitates in the samples aged for 15 h and 80 h, respectively. (at.%).

	Ageing condition	Mg	Zn	Gd	Zr
Spherical cluster	15 h.	61.47 ± 0.06	30.56 ± 0.05	7.14 ± 0.02	0.16 ± 0.01
	80 h.	59.37 ± 0.12	29.38 ± 0.09	9.26 ± 0.04	1.05 ± 0.04
Disc-shaped	80 h.	67.94 ± 0.03	21.75 ± 0.02	9.57 ± 0.01	0.12 ± 0.01

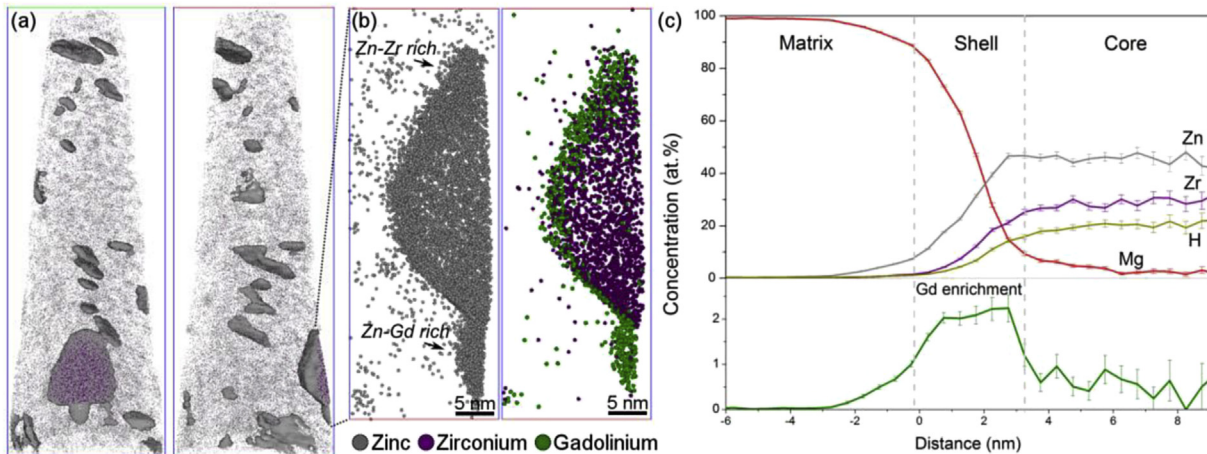


**Fig. 11.** Zr-rich precipitates with a core–shell structure in ZG52 alloy aged at 200 °C for 80 h. (a) Elemental map of the complete APT reconstruction. (b) Magnified slices within the precipitate. Zn, Zr and Gd atoms are represented as spheres. A Gd-rich shell was found to surround the Zn<sub>2</sub>Zr precipitate. (c) Proximity histogram showing the concentration profile constructed on a 7 at% Zn iso-concentration surface.

formation of Zr-rich phases also consumes Zn element from the solid solution, thus hinders the formation of Zn-rich phases and thereby reduces the age hardening response [8]. Two measures were very often taken to further improve mechanical properties. One is the addition of Zn in a high amount, i.e. 5 wt.% in the present investigation and ZK60 (the most commonly used Mg–Zn–Zr alloy). The other one is by using thermo-mechanical processing (i.e. extrusion and forging) to control grain size and improve the mechanical properties. However, recently, the beneficial effect of Zr-rich phase on the precipitation hardening was also reported [12,13], which was usually omitted in previous research. It has been reported that the nanoscale Zr-rich [0001]<sub>z</sub> rods/laths serve as favorable sites for heterogeneous nucleation of the Zn-rich β-type

phase and thereby enhance the precipitation hardening effect in a Mg–6Zn–0.5Cu–0.6Zr alloy during isothermal ageing at 180 °C [13]. It should be noted here that this proposal is fully consistent with our APT observation in Fig. 11, which provides a strong experimental support to the beneficial effect of Zr-rich phase on the heterogeneous nucleation of the Zn-rich β-type phase. Moreover, Zr-rich precipitates were also observed with a high number density. It may also cause the strengthening effect despite their large space and size. This suggestion is supported by the nanoscale mechanical properties analyses using nanoindentation and atomic force microscopy [39]. More importantly, Zn<sub>2</sub>Zr phase does not appear to coarsen even at elevated temperatures due to the formation of the core–shell structure (Fig. 11) and the low diffusivity of Zr (Table 5,

**Table 5**  
Diffusion of Mg, Zn, Gd, Zr in the Mg matrix at 200 °C [40–43].

Mg	Zn	Gd	Zr
$4 \times 10^{-20} \text{ m}^2 \text{ s}^{-1}$	$2.32 \times 10^{-19} \text{ m}^2 \text{ s}^{-1}$	$1.24 \times 10^{-9} \text{ m}^2 \text{ s}^{-1}$	–

not available as far as our knowledge). In order to show the size distribution of  $\text{Zn}_2\text{Zr}$  phase during ageing at 0.5 h, 15 h and 80 h, histograms are shown in Fig. 12, respectively. Clearly, a more uniform size distribution was obtained at ageing for 15 h. After ageing for 80 h, the length of  $\text{Zn}_2\text{Zr}$  phase increases, but the thickness decreases, which can be attributed to the preferable growth of  $\text{Zn}_2\text{Zr}$  phase along  $[0001]_Z$ , ensuring a minimal interface misfit between the  $\text{Zn}_2\text{Zr}$  phase and  $\alpha$ -Mg matrix.

#### 4.2. Precipitation of Zn-rich precipitates

In the Zr-lean regions, Zn-rich phases ( $\beta'_1$  phase and  $\beta'_2$  phase) were observed using TEM, as shown in Figs. 7 and 8. Furthermore, metastable GP zones, spherical clusters and disc-shaped precipitates were also observed using TEM and APT, respectively. As shown in Fig. 10a, at the initial condition (0.5 h), only fine compositional oscillations were observed, while, no precipitates

were observed. After ageing at 200 °C for 15 h, only spherical clusters (most likely  $\text{Mg}_2\text{Zn}$  phase, Fig. 10b) were observed using APT. It should be noted that  $\beta'_1$  phase and  $\beta'_2$  phase was also observed using TEM in this stage. After ageing at 200 °C for 80 h, not only spherical clusters but also disc-shaped precipitates (most likely  $\text{Mg}_2\text{Zn}$  phase, Fig. 10c) were observed using APT. Furthermore,  $\beta'_1$  phase and  $\beta'_2$  phase was also observed using TEM in this stage. Therefore, it is proposed that, in the Zr-lean regions, the precipitation of Zn-rich precipitates follows the process: spherical cluster  $\rightarrow$  disc-shaped metastable precipitates  $\rightarrow$  rod/plate-shaped  $\beta$  type precipitates ( $\beta'_1 \rightarrow \beta'_2$ )  $\rightarrow$  stable  $\beta$  precipitate (i.e.  $\text{MgZn}$ , not observed here). Instead, in the Zr-rich regions, the precipitation can be described as:  $\text{Zn}_2\text{Zr} \rightarrow$  rod/plate-shaped  $\beta$  type precipitates ( $\beta'_1 \rightarrow \beta'_2$ )  $\rightarrow$  stable  $\beta$  precipitate. Clearly, the precipitation of ZG52 alloy is dependent on the concentration of Zr, highlighting the importance of better understanding the formation of Zr-rich phase and its beneficial effect on heterogeneous nucleation of  $\beta$  type precipitates. It should be also noted that  $\beta$  type precipitates ( $\beta'_1$  and/or  $\beta'_2$ ) provide main strengthening effect on the alloy compared with  $\text{Zn}_2\text{Zr}$ , spherical cluster and disc-shaped metastable precipitates. However, controlling the formation of  $\text{Zn}_2\text{Zr}$ , spherical cluster and disc-shaped metastable precipitates significantly affects the heterogeneous nucleation of  $\beta$  type precipitates, and thereby their size and distribution as well as their strengthening effect on

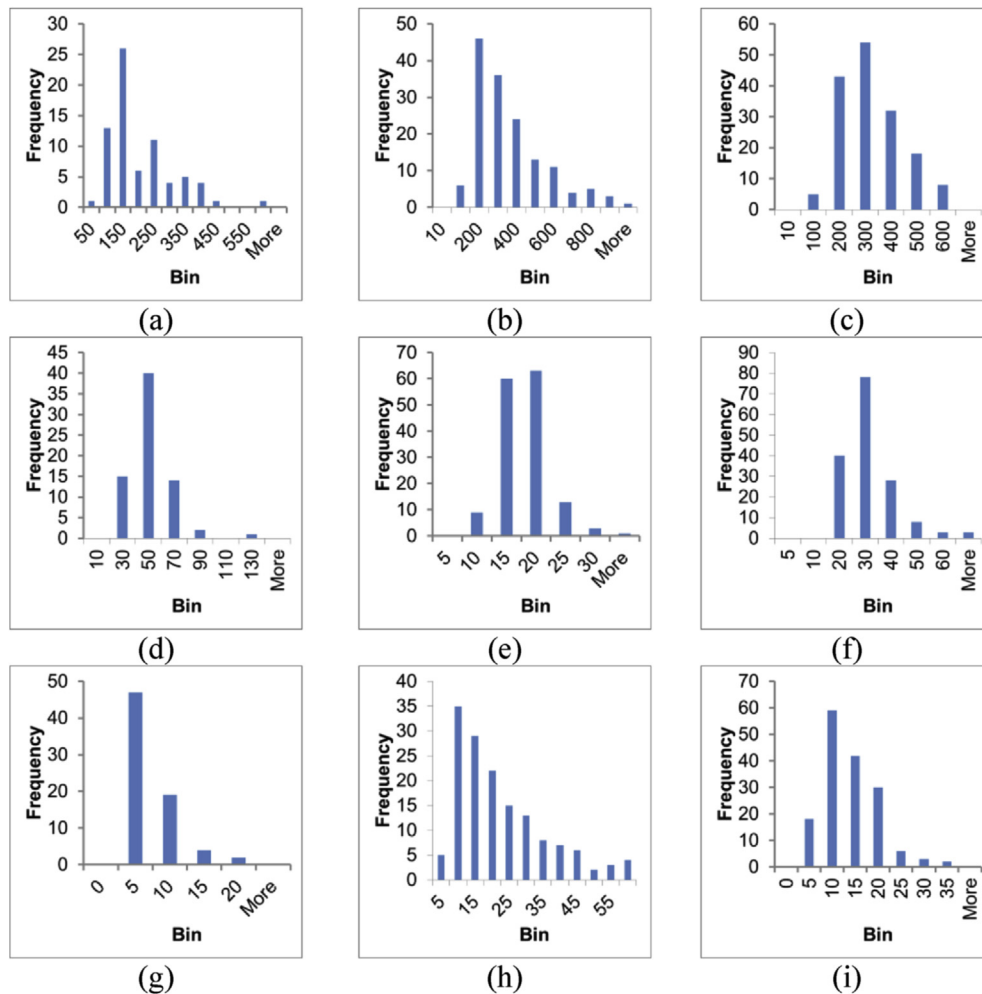


**Fig. 12.** Histograms showing the size distribution of  $\text{Zn}_2\text{Zr}$  phase during ageing from 0.5 h to 80 h. (a), (d), (g) for 0.5 h, (b), (e), (h) for 15 h, (c), (f), (i) for 80 h (a), (b), (c) for the length ( $L_R$ ), (d), (e), (f) for the width (or thickness) ( $W_R$ ), (g), (h), (i) for the ratio of the length ( $L_R$ ) and the width (or thickness) ( $W_R$ ). A more uniform size distribution and a large ratio of the length and the width (or thickness) were obtained at ageing for 15 h.

the alloy.

#### 4.3. Gd partitioning and its effect on precipitation

The diffusion of Gd ( $1.24 \times 10^{-9} \text{ m}^2 \text{ s}^{-1}$ ) [40,41] has been reported to be slower by about one order of magnitude than that of Mg ( $4 \times 10^{-20} \text{ m}^2 \text{ s}^{-1}$ ) and Zn ( $2.32 \times 10^{-19} \text{ m}^2 \text{ s}^{-1}$ ) [42,43] (Table 5), which is believed to be due to the larger atomic size of Gd compared to those of Mg and Zn [40]. Such slow diffusion of Gd in Mg can be expected to be a rate-limiting factor to control the precipitation behavior.

The partitioning of Gd into the Zr-rich particles (0.5 at%) was observed, as shown in Fig. 11. More importantly, a core–shell structure with the shell of Gd (2 at%) and the core of  $\text{Zn}_2\text{Zr}$  phase was observed. The formation of the core–shell structure can be attributed to the fact that the formation of Zr-rich phases gradually consumes Zn and Zr from the solid solution, leading to a Zn,Zr-lean region in the vicinity of Zr-rich phase. It is the Zn,Zr-lean region that accelerates the diffusion or partitioning of Gd toward the Zr-rich phases, forming the core–shell structure. The formation of the core–shell structure is proposed to reduce the stain between Zr-rich phases and  $\alpha$ -Mg matrix, hinder the coarsening of Zr-rich phases (Fig. 12) and thereby increase its strengthening effect.

The partitioning of Gd into the Zn-rich phase was also observed, as shown in Fig. 10c. When aged for 15 h, a significant partitioning of Gd into Zn-rich phase (spherical cluster) was observed. With increasing ageing time (up to 80 h), more Gd was observed in Zn-rich phase (spherical cluster and disc-shaped precipitates). Although no significant partitioning of Gd into  $\beta$  type precipitates ( $\beta_1'$  and/or  $\beta_2'$ ) was observed in present investigation, similar to the case of  $\text{Zn}_2\text{Zr}$  phases, the formation and/or growth of the  $\beta$  type precipitates ( $\beta_1'$  and/or  $\beta_2'$ ) also gradually consume Zn from the solid solution, leading to a Zn-lean region in the vicinity of  $\beta$  type precipitates ( $\beta_1'$  and/or  $\beta_2'$ ). It is the Zn-lean region that accelerates the diffusion or partitioning of Gd toward the Zn-rich precipitates, reduces the stain between Zn-rich precipitates and  $\alpha$ -Mg matrix, and thereby improves the stability of Zn-rich precipitates. It should be noted here that the  $\text{Zn}_2\text{Zr}$  particles themselves also gradually decompose during the precipitation of Zn-rich precipitates, releasing Zr atoms and diffusing into the matrix or involving into the formation of new Zr-containing compounds. However, the diffusion of Zr (Table 5, not available as far as our knowledge) is expected to be much slower than that of other elements (Mg, Zn, Gd). Although the partitioning of Gd into the Zn-rich phase does not appear to produce a significant effect on the precipitation process (as discussed in section 4.2), it may improve the thermal stability of the Zn-rich phase and finally enhances the precipitation hardening of ZG52 alloy, as shown in Fig. 2.

## 5. Summary

- (1) The precipitation process involves the formation of precipitates with different morphologies and habit planes: triangular-shaped ZnZr phase, rectangular-shaped  $\text{Zn}_2\text{Zr}$  phase,  $[0001]_{\text{Mg}}$  rods ( $\beta_1'$ ) MgZn<sub>2</sub> Laves phase,  $(0001)_{\text{Mg}}$  plate ( $\beta_2'$ ) MgZn<sub>2</sub> Laves phase and coherent GP zones.
- (2) No significant coarsening of Zn-rich precipitates ( $\beta_1'$  and  $\beta_2'$ ) was observed, even after ageing at 200 °C for 80 h, indicating the partitioning of Gd into Zn-rich precipitates improves their thermal stability and thereby enhances the precipitation hardening.
- (3) A core–shell structure with the shell of Gd (2 at%) and the core of  $\text{Zn}_2\text{Zr}$  phase was observed, which is proposed to hinder the coarsening of  $\text{Zn}_2\text{Zr}$  phase. No further change in

average size of the  $\text{Zn}_2\text{Zr}$  particles was observed after ageing over 15 h.

- (4) This investigation demonstrates that it is of great necessity to elucidate the partitioning of Gd into the Zr-rich precipitates and Zn-rich precipitates, which can be used to tailor the precipitation hardening and thereby design high performance Mg alloys.

## Acknowledgments

The author (J.H. Li) acknowledges the access to TEM instruments at the Erich Schmidt Institute of Materials Science of the Austrian Academy of Science and the financial support from the Major International (Regional) Joint Research Project (No. 51420105005) from China and the Eurasia-Pacific Uninet project (EPU 06/2015). The authors (J. Barrirero, H. Aboulfadl, F. Mücklich) gratefully acknowledge the EU funding in the framework of the project AME-Lab (European Regional Development Fund C/4-EFRE-13/2009/Br). The Atom Probe was financed by the DFG and the Federal State Government of Saarland (INST 256/298-1 FUGG). J. Barrirero acknowledges the Erasmus Mundus Doctoral Programme DocMASE of the European Commission.

## References

- [1] B. Smola, I. Stulíková, F. von Buch, B.L. Mordike, Structural aspects of high performance Mg alloys design, *Mater. Sci. Eng. A* 324 (2002) 113–117.
- [2] J.B. Clark, L. Zabdyyr, Z. Moser, in: A.A. Nayeb-Hashemi, J.B. Clark (Eds.), *Phase Diagram of Binary Magnesium Alloys*, ASM International, Metals Park, OH, 1988, p. 353.
- [3] J.B. Clark, Transmission electron microscopy study of age hardening in a Mg-5 wt.% Zn alloy, *Acta Metall.* 13 (1965) 1281–1289.
- [4] J. Buha, Reduced temperature (22–100 °C) ageing of an Mg–Zn alloy, *Mater. Sci. Eng. A* 492 (2008) 11–19.
- [5] X. Gao, J.F. Nie, Structure and thermal stability of primary intermetallic particles in an Mg–Zn casting alloy, *Scr. Mater.* 57 (2007) 655–658.
- [6] D. StJohn, M.A. Qian, M.A. Easton, P. Cao, Z. Hidebrand, Grain refinement of magnesium alloys, *Metall. Mater. Trans. A* 36A (2005) 1669–1679.
- [7] Z. Hidebrand, M.A. Qian, D. StJohn, M. Frost, Influence of zinc on the soluble zirconium content in magnesium and the subsequent grain refinement by zirconium, in: A.A. Luo (Ed.), *Magnesium. Technology 2004*, Minerals, Metals & Materials Society (TMS), Warrendale, PA, U.S.A., 2004, pp. 241–245.
- [8] J.D. Robson, C. Paa-Rai, The interaction of grain refinement and ageing in magnesium–zinc–zirconium (ZK) alloys, *Acta Mater.* 95 (2015) 10–19.
- [9] G.I. Morozova, I.Yu. Mukhina, Nanostructural hardening of cast magnesium alloys of the Mg–Zn–Zr system, *Metal Sci. Heat Treat.* 53 (2011) 3–7.
- [10] J. Buha, The effect of micro-alloying addition of Cr on age hardening of an Mg–Zn alloy, *Mater. Sci. Eng. A* 492 (2008) 293–299.
- [11] J. Buha, Mechanical Properties of Naturally Aged Mg–Zn–Cu–Mn Alloy, *Mater. Sci. Eng. A* 489 (2008) 127–137.
- [12] G. Sha, H.M. Zhu, J.W. Liu, C.P. Luo, Z.W. Liu, S.P. Ringer, Hydrogen-induced decomposition of Zr-rich cores in an Mg–6Zn–0.6Zr–0.5Cu alloy, *Acta Mater.* 60 (2012) 5615–5625.
- [13] H.M. Zhu, G. Sha, J.W. Liu, C.L. Wu, C.P. Luo, Z.W. Liu, R.K. Zheng, S.P. Ringer, Microstructure and mechanical properties of Mg–6Zn–xCu–0.6Zr (wt.%) alloys, *J. Alloys Compd.* 509 (2011) 3526–3531.
- [14] H.M. Zhu, G. Sha, J.W. Liu, H.W. Liu, C.L. Wu, C.P. Luo, Z.W. Liu, R.K. Zheng, S.P. Ringer, Heterogeneous nucleation of  $\beta$ -type precipitates on nanoscale Zr-rich particles in a Mg–6Zn–0.5Cu–0.6Zr alloy, *Nanoscale Res. Lett.* 7 (2012) 300.
- [15] J. Buha, The effect of Ba on the microstructure and age hardening of an Mg–Zn alloy, *Mater. Sci. Eng. A* 491 (2008) 70–79.
- [16] G. Ben-Hamu, D. Eliezer, A. Kaya, Y.G. Na, K.S. Shin, Microstructure and corrosion behavior of Mg–Zn–Ag alloys, *Mater. Sci. Eng. A* 435–436 (2006) 579–587.
- [17] C.J. Bettles, M.A. Gibson, K. Venkatesan, Enhanced age-hardening behaviour in Mg–4 wt.% Zn micro-alloyed with Ca, *Scr. Mater.* 51 (2004) 193–198.
- [18] C.L. Mendis, K. Oh-ishi, K. Hono, Enhanced age hardening in a Mg–2.4 at% Zn alloy by trace additions of Ag and Ca, *Scr. Mater.* 57 (2007) 485–488.
- [19] C.L. Mendis, K. Oh-ishi, Y. Kawamura, T. Honma, S. Kamado, K. Hono, Precipitation-hardenable Mg–2.4Zn–0.1Ag–0.1Ca–0.16Zr (at.%) wrought magnesium alloy, *Acta Mater.* 57 (2009) 749–760.
- [20] J. Buha, Grain refinement and improved age hardening of Mg–Zn alloy by a trace amount of V, *Acta Mater.* 56 (2008) 3533–3542.
- [21] B. Rashkova, W. Prantl, R. Görgl, J. Keckes, S. Cohen, M. Bamberger, G. Dehm, Precipitation processes in a Mg–Zn–Sn alloy studied by TEM and SAXS, *Mater. Sci. Eng. A* 494 (2008) 158–165.

- [22] A. Singh, A.P. Tsai, Structural characteristics of  $\beta 1'$  precipitates in Mg–Zn-based alloys, *Scr. Mater.* 57 (2007) 941–944.
- [23] J. Yang, J.L. Wang, L.D. Wang, Y.M. Wu, L.M. Wang, H.J. Zhang, Microstructure and mechanical properties of Mg–4.5Zn–xNd ( $x = 0, 1$  and  $2$ , wt%) alloys, *Mater. Sci. Eng. A* 479 (2008) 339–344.
- [24] S.M. He, L.M. Peng, X.Q. Zeng, W.J. Ding, Y.P. Zhu, Comparison of the microstructure and mechanical properties of a ZK60 alloy with and without 1.3 wt.% gadolinium addition, *Mater. Sci. Eng. A* 433 (2006) 175–181.
- [25] J. Yang, W.L. Cio, L.D. Wang, Y.M. Wu, L.M. Wang, H.J. Zhang, Influences of Gd on the microstructure and strength of Mg–4.5Zn alloy, *Mater. Charact.* 59 (2008) 1667–1674.
- [26] S.J. Liu, G.Y. Yang, S.F. Luo, W.Q. Jie, Microstructure and mechanical properties of sand mold cast Mg–4.58Zn–2.6Gd–0.18Zr magnesium alloy after different heat treatments, *J. Alloys Compd.* 644 (2015) 846–853.
- [27] J. Yang, L.D. Wang, L.M. Wang, H.J. Zhang, Microstructures and mechanical properties of the Mg–4.5Zn–xGd ( $x = 0, 2, 3$  and  $5$ ) alloys, *J. Alloys Compd.* 459 (2008) 274–280.
- [28] H.Y. Yu, H.G. Yan, J.H. Chen, B. Su, Y. Zheng, Y.J. Shen, Z.J. Ma, Effects of minor Gd addition on microstructures and mechanical properties of the high strain-rate rolled Mg–Zn–Zr alloys, *J. Alloys Compd.* 586 (2008) 757–765.
- [29] L.Y. Wei, G.L. Dunlop, H. Westengen, Precipitation hardening of Mg–Zn and Mg–Zn–RE alloys, *Metall. Mater. Trans. A* 26A (1995) 1705–1716.
- [30] L.Y. Wei, G.L. Dunlop, H. Westengen, The intergranular microstructure of cast Mg–Zn and Mg–Zn–rare earth alloys, *Metall. Mater. Trans. A* 26A (1995) 1947–1955.
- [31] B.Q. Chen, J. Zhang, Microstructure and mechanical properties of ZK60–Er magnesium alloys, *Mater. Sci. Eng. A* 633 (2015) 154–160.
- [32] K. Thomson, D. Lawrence, D.J. Larson, J.D. Olson, T.F. Kelly, B. Gorman, In situ site-specific specimen preparation for atom probe tomography, *Ultra-microscopy* 107 (2007) 131–139.
- [33] E.A. Marquis, J.M. Hyde, Applications of atom-probe tomography to the characterisation of solute behaviours, *Mater. Sci. Eng. R* 69 (2010) 37–62.
- [34] R. Arroyave, A. Walle, Z.K. Liu, First-principles calculations of the Zn–Zr system, *Acta Mater.* 54 (2006) 473–482.
- [35] H.J. Blythe, A. Physics Letters, Ferromagnetism in the system  $(Zr_{1-x}Hf_x)Zn_2$  27 (1968) 42–43.
- [36] X. Gao, J.F. Nie, Characterization of strengthening precipitate phases in a Mg–Zn alloy, *Scr. Mater.* 56 (2007) 645–648.
- [37] T.F. Kelly, M.K. Miller, Invited review article: Atom probe tomography, *Rev. Sci. Instrum.* 78 (2007) 031101.
- [38] B. Gault, M.P. Moody, J.M. Cairney, S.P. Ringer, *Atom Probe Microscopy*, Springer New York, New York, NY, 2012.
- [39] D. Shepelev, M. Bamberger, A. Katsman, Precipitation hardening of Zr-modified Mg–Ca–Zn alloy, *J. Mater. Sci.* 44 (2009) 5627–5635.
- [40] S.K. Das, Y.B. Kang, T.K. Ha, I.H. Jung, Thermodynamic modeling and diffusion kinetic experiments of binary Mg–Gd and Mg–Y systems, *Acta Mater.* 71 (2014) 164–175.
- [41] L. Huber, I. Elfimov, J. Rottler, M. Militzer, Ab initio calculations of rare-earth diffusion in magnesium, *Phys. Rev. B* 85 (2012) 144301.
- [42] S.K. Das, Y.M. Kim, T.K. Ha, I.H. Jung, Investigation of anisotropic diffusion behavior of Zn in hcp Mg and interdiffusion coefficients of intermediate phases in the Mg–Zn system, *CALPHAD* 42 (2013) 51–58.
- [43] S. Ganeshan, L.G. Hector Jr., Z.K. Liu, First-principles calculations of impurity diffusion coefficients in dilute Mg alloys using the 8-frequency model, *Acta Mater.* 59 (2011) 3214–3228.